Available online at www.sciencedirect.com
ScienceDirect
Journal of Solid State Chemistry 180 (2007) 1277–1290
JOURNAL OF SOLID STATE CHEMISTRY
www.elsevier.com/locate/jssc

$CeAlO_3$ and $Ce_{1-x}R_xAlO_3$ (R = La, Nd) solid solutions: Crystal structure, thermal expansion and phase transitions

L. Vasylechko[a,*], A. Senyshyn[a,b], D. Trots[b], R. Niewa[c,d], W. Schnelle[c], M. Knapp[b,e]

[a]*Institute of Telecommunications, Radioelectronics and Electronics Technique, Semiconductor Electronics Department, Lviv Polytechnic National University, 12 Bandera Street, 79013 Lviv, Ukraine*
[b]*Materialwissenschaft, Technische Universität Darmstadt, Petersenstraße 23, 64287 Darmstadt, Germany*
[c]*Max-Planck-Institut für Chemische Physik fester Stoffe, Nöthnitzer Straße 40, 01187 Dresden, Germany*
[d]*Department Chemie, Technische Universität München, Lichtenbergstraße 4, 85747 Garching b. München, Germany*
[e]*CELLS, POB 68, 08193, Barcelona, Spain*

Received 17 November 2006; received in revised form 15 January 2007; accepted 17 January 2007
Available online 1 February 2007

Abstract

The crystal structures of $CeAlO_3$ and the solid solutions $Ce_{1-x}R_xAlO_3$ (R = La, Nd), and their thermal behaviour in a wide temperature range of 12−1200 K have been precisely determined by means of *in situ* high-resolution X-ray powder diffraction technique applying synchrotron radiation, thermal analysis and magnetic measurements. The unique sequence of the reversible phase transitions $I4/mcm \leftrightarrow Imma \leftrightarrow R\bar{3}c \leftrightarrow Pm\bar{3}m$ has been detected in $CeAlO_3$ and solid solutions formed in the pseudo-binary system $CeAlO_3$–$LaAlO_3$. In the $Ce_{1-x}Nd_xAlO_3$ system, the samples with $x = 0.3$ and 0.5 compositions undergo three phase transformations $I2/m \leftrightarrow Imma \leftrightarrow R\bar{3}c \leftrightarrow Pm\bar{3}m$, whereas for the Ce-rich sample $Ce_{0.9}Nd_{0.1}AlO_3$ four successive transitions are observed: $I4/mcm \leftrightarrow I2/m \leftrightarrow Imma \leftrightarrow R\bar{3}c \leftrightarrow Pm\bar{3}m$. Crystal structure parameters of all structural polymorphs of $CeAlO_3$ and solid solutions based on them as well as their thermal evolution are reported. Based on *in situ* powder diffraction and DTA/DSC data, the phase diagrams of the pseudo-binary systems $CeAlO_3$–$LaAlO_3$ and $CeAlO_3$–$NdAlO_3$ are constructed together with a combined phase diagram, where the transition temperatures are presented as a function of the average radius of rare-earth cations.

Keywords: $CeAlO_3$; $CeAlO_3$–$LaAlO_3$ and $CeAlO_3$–$NdAlO_3$ systems; Perovskite; Crystal structure; Phase transition; Thermal expansion; Phase diagram

1. Introduction

At room temperature (RT), the majority of $RAlO_3$ aluminates belong to the two widespread types of distorted perovskite structures, namely $LaAlO_3$ (space group (SG) $R\bar{3}c$, R = La, Pr, Nd) and $GdFeO_3$ (SG $Pbnm$, R = Sm–Lu, Y) [1–5]. The sole exception among $RAlO_3$ compounds is $CeAlO_3$. For the first time the structure of cerium aluminate was reported in 1949 by Zachariasen [6] to be tetragonal, with a weak elongation in one of the cubic perovskite axes. Later a variety of hexagonal [7], trigonal [8–10] and cubic [11] structures of $CeAlO_3$ have been reported. However, the later data reported by Kaufherr et al. [12] and single-crystal diffraction investigations performed by Tanaka et al. [13] in 1993 assigned a simple tetragonal structure for $CeAlO_3$ (SG $P4/mmm$, $a = 3.7669$ Å, $c = 3.7967$ Å), as it was initially proposed by Zachariasen. This structure was commonly approved for cerium aluminate in the last decade [3,14–18]. Only in Ref. [19], the growth of orthorhombic $CeAlO_3$ single crystal with the lattice parameters $a_1 = 5.316(1)$, $a_2 = 5.314(1)$ and $c = 7.576(1)$ Å, close to a cubic system, was reported.

First information on the phase transformations in $CeAlO_3$ has been reported in the 1960th. Leonov et al. [20] and Leonov [21] observed two phase transitions in $CeAlO_3$ using optical methods: to a rhombohedral phase at 363 K and to a cubic one at 1253 K. Geller and Raccah [22] have predicted the rhombohedral-to-cubic transition in

*Corresponding author. Fax: +38 032 2744300.
E-mail address: crystal-lov@polynet.lviv.ua (L. Vasylechko).

0022-4596/$ - see front matter © 2007 Elsevier Inc. All rights reserved.
doi:10.1016/j.jssc.2007.01.020

$CeAlO_3$ at 1230 K from the extrapolation of corresponding transition temperatures in the related $RAlO_3$ (R = La, Pr, Nd) compounds. More recently, Egorov et al. [23] in their publication devoted to the phase transformations in $BaCeO_3$, have reported on two phase transformations in $CeAlO_3$ at ca. 310 and ca. 450 K using DTA. Electrical and optical properties of $CeAlO_3$ single crystals have been studied in Ref. [17]. The authors confirmed the phase transformations at 310 and 440 K as well as the high-temperature (HT) transition to the optically isotropic cubic phase, which starts at 1170 K and finishes at about 1400 K. A thermal hysteresis of about 100 K has been observed. However, neither information on the structural peculiarities of different modifications of $CeAlO_3$ nor on their thermal behaviour has been reported in the aforementioned publications.

The first results of a structural investigation of $CeAlO_3$ in a wide temperature range of 12–1230 K were published in 2002 [24–26]. *In situ* examination of the structure using high-resolution powder diffraction technique with very high signal-to-noise ratio reveals the presence of several weak superstructure reflections, which could not be indexed in a simple tetragonal perovskite-like cell. Accordingly, the $CeAlO_3$ structure at RT has been refined in SG $I4/mcm$ with the $\sqrt{2}a_p \times \sqrt{2}a_p \times 2a_p$ lattice. Somewhat later, the same RT structure of $CeAlO_3$ was confirmed in [27]. Based on *in situ* synchrotron powder diffraction examinations and DTA/DSC studies [24–26] it was shown that $CeAlO_3$ undergoes a sequence of structural phase transformations: $I4/mcm \leftrightarrow Imma$ at 314 K, $Imma \leftrightarrow R\bar{3}c$ at 430 K and $R\bar{3}c \leftrightarrow Pm\bar{3}m$ at 1250 K. Crystal structure parameters of all structural modifications of $CeAlO_3$ including atomic coordinates, have been refined and published [26]. Just recently, the same phase transformations in $CeAlO_3$ have been observed independently applying *in situ* time-of-flight neutron powder diffraction [28].

The observed sequence of phase transitions in $CeAlO_3$ is unique among all AMO_3 compounds with perovskite structures. A similar complicated phase behaviour was observed only for praseodymium aluminate. According to the literature data, $PrAlO_3$ undergoes a continuous phase transition $R\bar{3}c \leftrightarrow Pm\bar{3}m$ at 1864 K, a first-order transformation $Imma \leftrightarrow R\bar{3}c$ at 205 K and a second-order transition $C2/m(I2/m) \leftrightarrow Imma$ at 150 K [29–35]. In Refs. [30–31,33], an additional low-temperature (LT) transition in $PrAlO_3$ at 118 K was reported, which is caused by the coupling of acoustic phonons with the temperature-dependent optical modes. This second-order transition should be accompanied by symmetry change; however, it was not confirmed by X-ray or neutron diffraction investigations [34,35]. According to [35], the acoustic anomaly observed in [30,33] appears to be associated with a metrically tetragonal structure, which develops an accidental strain degeneracy in the temperature range of 110–120 K.

In order to study the influence of cation substitution on the phase transition in $CeAlO_3$, a set of $Ce_{1-x}R_xAlO_3$ samples (R = La, Nd, Pr) was prepared and investigated. Preliminary results on the structure and thermal expansion of the solid solutions and phase diagrams of the $CeAlO_3$–$RAlO_3$ (R = La, Nd, Pr) pseudo-binary systems were reported in Refs. [26,36–39] in brief. In the present work, the results on the study of crystal structures, its thermal and magnetic behaviour and especially the phase transformations are summarized and analyzed for the case of cerium aluminate, $Ce_{1-x}La_xAlO_3$ and $Ce_{1-x}Nd_xAlO_3$ solid solutions. The influence of cation substitution on the phase transitions in $CeAlO_3$ is discussed.

2. Experimental

2.1. Sample preparation

Samples of $CeAlO_3$ and $Ce_{1-x}R_xAlO_3$ solid solutions with $x = 0.1, 0.3, 0.5, 0.7, 0.9$ for La and $x = 0.1, 0.3, 0.5, 0.7, 0.8$ and 0.9 for Nd were obtained from the oxide precursors CeO_2, La_2O_3, Nd_2O_3 and Al_2O_3 according to the following reactions:

$$2CeO_2 + Al_2O_3 = 2CeAlO_3 + 1/2O_2,$$

$$2(1-x)CeO_2 + xR_2O_3 + Al_2O_3 = 2Ce_{1-x}R_xAlO_3 + 1/2\ (1-x)O_2.$$

Previously annealed oxides were weighted in appropriate molar ratios and ball milled for 4 h using ethanol medium. The obtained mixtures were dried and pressed to pellets.

Initially, the synthesis of $CeAlO_3$ was performed by solid-state reaction in vacuum at 1470 K. The pellet of the oxide mixture was contained in an alumina crucible, wrapped in a protective Ta-foil, sealed in evacuated quartz tube and than annealed at 1470 K for 48 h. XRD examination of the sample obtained showed almost single-phase perovskite; the amount of CeO_2 did not exceed 3–5 wt%. The observed value of effective magnetic moment (2.44 μ_B) obtained from the magnetic susceptibility measurement confirms the predominant presence of Ce^{3+} in the sample (vide infra). A somewhat modified approach for the synthesis of Ce-containing aluminates was applied to improve phase purity. The pressed pellets were sintered in a dynamic vacuum at 1670−1770 K for 1 h. Thereafter, the samples were arc melted in a purified Ar atmosphere. By using this technique, pure perovskite samples of $CeAlO_3$ and $Ce_{1-x}R_xAlO_3$ solid solutions were obtained. Only negligible amounts of CeO_2 have been detected in a separate samples from $CeAlO_3$–$NdAlO_3$ pseudo-binary system.

2.2. Sample characterization

For XRD phase analysis, a Huber image plate Guinier camera G670 with monochromated Cu$K\alpha_1$ radiation (λ = 1.54056 Å) and a DRON-3M powder diffractometer were used. Phase purity was examined for both sintered

and arc-melted samples. *In situ* LT and HT powder diffraction investigations have been carried out at the experimental station B2 in synchrotron laboratory HASYLAB at DESY (Hamburg, Germany). Both LT and HT diffraction experiments were performed in the Debye–Scherrer capillary geometry using an on-site readable image plate detector OBI [40]. The typical full width at half maximum (FWHM) of reflections of the diffraction patterns obtained in this geometry with image plate detector was 0.06−0.08°. Besides, in order to get better resolution and signal-to-noise ratio, some diffraction patterns were collected in reflection mode (Bragg–Brentano geometry) using a NaI scintillation detector and analyzer crystal. This allows us to achieve a very high resolution with typical FWHM values of 0.03−0.04° for the samples. A closed-cycle cryostat [41] and a STOE furnace were used for *in situ* LT and HT diffraction experiments. In all experiments, the wavelength was calibrated using the reflection positions of silicon (NIST SRM 640b) and/or LaB_6 (NIST SRM 660a) reference materials. Details of the synchrotron diffraction experiments are given elsewhere [24,36–38].

Data analysis and all crystallographic calculations (refinement of the lattice parameters, full profile Rietveld structure refinement) were performed within the WinCSD programme package [42].

Thermal analysis of the samples was carried out using a simultaneous DTA/TG procedure (STA 409 C, Netzsch) with alumina crucibles under air and flowing argon (75 ml/min, Messer Griesheim 5.0, additionally purified with Oxysorb) with the heating rate of 10 K/min up to maximal temperature of 1723 K. The temperature range of 170–673 K was covered using a DSC 204 Phoenix (Netzsch) with sealed aluminium crucibles with life heating rates (5, 10, 20 K/min). The data were extrapolated to a heating rate of 0 K/min. The systems were calibrated using five melting standards.

Magnetic susceptibility on bulk material was measured in a SQUID magnetometer (Quantum Design, MPMS-XL7) in the temperature range 1.8–400 K in fields of 10 and 1 kOe (in the latter field with both increasing and decreasing temperature).

3. Results

3.1. Crystal structure and phase transitions in $CeAlO_3$

Thermal analysis of the $CeAlO_3$ sample confirmed well-known literature data on its thermal instability in air and the stability in inert atmosphere. Simultaneous DTA/TG measurements performed in air demonstrate that the oxidation of $CeAlO_3$ starts at 1239 K; the corresponding exothermic peak has a maximum at 1363 K. Decomposition of cerium aluminate into CeO_2 and Al_2O_3 was proved by XRD analysis of the sample after DTA. DTA/TG investigations performed in Ar atmosphere reveal no change of mass but two endothermic peaks at 310 and 430 K, both comparably broad and with small enthalpy. These peaks point on the phase transformations occurring in $CeAlO_3$. *In situ* high-resolution powder diffraction experiments confirmed these observations. Changes in the character of reflections splitting observed in the temperature ranges of 300–330 and 403–503 K, and the temperature dependencies of the lattice parameters obtained (Fig. 1) clearly prove the presence of structural phase transitions at these temperatures. LT examinations of $CeAlO_3$ demonstrated that the tetragonal structure remains stable above 12 K at least. Neither extra reflection splitting/shape deformation, nor appearance of additional superstructure reflections was observed, even using the HRPD technique with very high signal-to-noise ratio. On the other hand, an extremely high collimation of synchrotron beam allowed us to observe an anisotropic broadening of some diffraction maxima normally undistinguishable with conventional X-ray sources. The deformation, clearly visible at RT, diminishes with the temperature decrease and disappears completely below 220 K. This observation could be explained by the effect of incipient orthorhombic phase owing to the forthcoming phase transition at 300–330 K. Co-existence of LT tetragonal and HT orthorhombic phases has been also found at the diffraction patterns

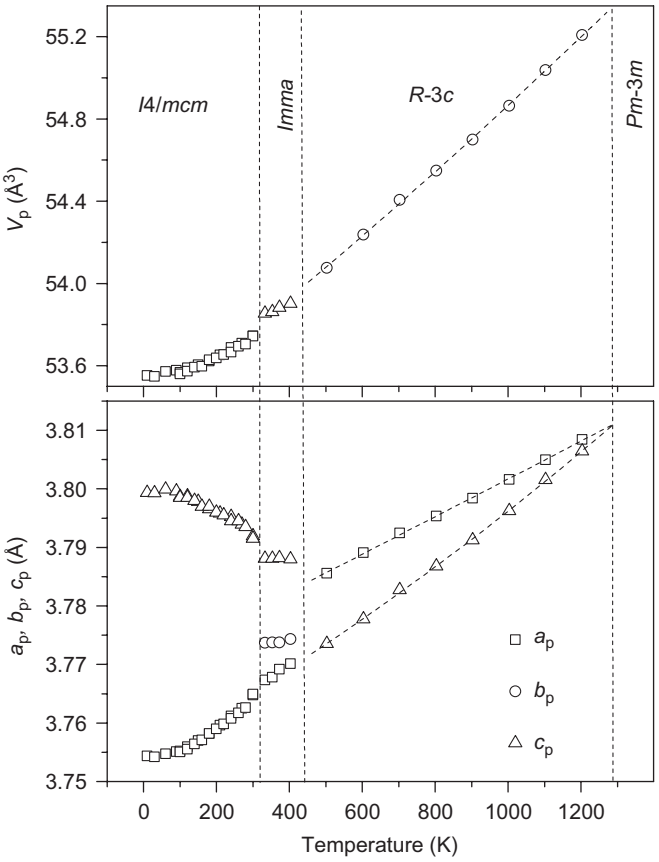

Fig. 1. Temperature dependency of the lattice parameters and cell volume of $CeAlO_3$. Lattice parameters of the tetragonal, orthorhombic and rhombohedral phases are transformed into perovskite-like pseudo-cells as follows: $a_p = a_t/\sqrt{2}$, $c_p = c_t/2$, $V_p = V_t/4$; $a_p = a_o/\sqrt{2}$, $b_p = b_o/2$, $c_p = c_o/\sqrt{2}$, $V_p = V_o/4$; $a_p = a_r/\sqrt{2}$, $c_p = c_r/\sqrt{12}$, $V_p = V_r/6$.

collected at 313, 333 and 353 K, which is a typical indicator for a first-order phase transition.

An orthorhombic $CeAlO_3$ structure exists in a narrow temperature range of 314–430 K. With increasing temperature, it transforms into a rhombohedral one. The temperature behaviour of the perovskite-like lattice parameters of the rhombohedral phase, which approach each other and become equal at temperatures above 1200 K (Fig. 1), point on another phase transformation from the rhombohedral to the cubic phase. Temperature of this continuous transition (1288 K) could be estimated from the extrapolation of the cell parameters ratio and it is close to one obtained in [26] from the analysis of the octahedral tilt angles (1262 K). Somewhat higher transition temperature was reported in Ref. [28]. Based on the observation of residual superlattice reflections at neutron powder diffraction patterns, the authors concluded the existence of rhombohedral-to-cubic transition in $CeAlO_3$ at 1373 K. All these observations agree well with the recently published optical investigations of $CeAlO_3$ single crystals [17], where the continuous transition to an isotropic cubic phase was approved to take place in the temperature region 1170–1400 K. The Rietveld refinement of the $CeAlO_3$ structure at the maximum available temperature for the used furnace (1203 K) reveals that the HT structure could be successfully refined either in rhombohedral or in cubic structure with residuals being almost the same (Table 1, Fig. 2). Final results of the structure refinements of different $CeAlO_3$ polymorphs performed in SGs $I4/mcm$, $Imma$, $R\bar{3}c$ and $Pm\bar{3}m$ are presented in Table 1 and in Fig. 2. Distribution of the selected interatomic distances and angles along with their temperature dependencies presented in Fig. 3 reflect the structural peculiarities of different modifications of $CeAlO_3$ and the changes occurred at the phase transitions.

An increase in temperature leads to a decrease of the perovskite structure deformation, which is demonstrated by the upward trend in observed tolerance factors t_o, calculated for different possible coordination numbers (CN) of Ce cations (Fig. 4a). The latter criterion was proposed by Sasaki et al. [43] as a measure of structure deformation, arising from the tilts and/or distortion of polyhedra in perovskite structures. It was defined as follows: $t_o = (AO)_{12}/\sqrt{2}(MO)_6$, where $(AO)_{12}$ and $(MO)_6$ are the average interatomic distances in the respective polyhedra. Analysis of the *bond-length distortion* Δ, calculated according to [43] for the corresponding polyhedra (Fig. 4b and c) also confirms the downward tendency for a perovskite structure deformation in $CeAlO_3$ with the temperature rising.

3.2. $CeAlO_3$–$RAlO_3$ systems (R = La, Nd)

3.2.1. Structure and thermal behaviour of $Ce_{1-x}La_xAlO_3$ and $Ce_{1-x}Nd_xAlO_3$ solid solutions

XRD examinations of $Ce_{1-x}R_xAlO_3$ samples at RT showed that the specimens with $x = 0.1$ and 0.3 possess the orthorhombic perovskite-type structure, whereas for the compositions with $x \geqslant 0.5$ the rhombohedral deformation of the perovskite lattice is observed. *In situ* synchrotron powder diffraction investigations revealed HT cubic and LT tetragonal modifications of $Ce_{1-x}La_xAlO_3$ solid solutions existing in the $CeAlO_3$–$LaAlO_3$ pseudo-binary system. The sequence of the phase transitions detected in $Ce_{1-x}La_xAlO_3$ samples is identical to one observed in $CeAlO_3$. Significant decrease of all transition temperatures is observed with decreasing cerium concentration in the corresponding samples.

The $CeAlO_3$–$NdAlO_3$ system exhibits a more complex behaviour. In contrast to the previously discussed system, the LT modifications of $Ce_{1-x}Nd_xAlO_3$ solid solutions display a monoclinic deformation of the perovskite structure, and the tetragonal LT structure is observed only for a Ce-rich $Ce_{0.9}Nd_{0.1}AlO_3$ sample. *In situ* HT investigations performed in the temperature range of 298−1173 K did not reveal a transition from rhombohedral to cubic structure, but taking into account a continuous character of this transition, it could be predicted from the temperature dependencies of the rhombohedral lattice parameters and their ratio. Thus, $Ce_{1-x}Nd_xAlO_3$ samples with $x = 0.3$ and 0.5 undergo a sequence of the phase transformations $I2/m \leftrightarrow Imma \leftrightarrow R\bar{3}c \leftrightarrow Pm\bar{3}m$, similar to those described in the literature for the praseodymium aluminate $PrAlO_3$ [34,35]. For a $Ce_{0.9}Nd_{0.1}AlO_3$ sample three LT phase transitions are observed: $I4/mcm \leftrightarrow I2/m$ at 205 K, $I2/m \leftrightarrow Imma$ at 263 K, and $Imma \leftrightarrow R\bar{3}c$ at 405 K. A fourth HT transition to the cubic structure is predicted to occur at 1360 K.

The thermal behaviour of the lattice parameters in $Ce_{1-x}R_xAlO_3$ solid solutions on examples of $Ce_{0.1}La_{0.9}AlO_3$, $Ce_{0.5}La_{0.5}AlO_3$, $Ce_{0.5}Nd_{0.5}AlO_3$ and $Ce_{0.7}Nd_{0.3}AlO_3$ samples is presented in Fig. 5. Temperature dependencies of the cell volumes for all studied $Ce_{1-x}R_xAlO_3$ samples are collected in Fig. 6. Besides, the temperature and concentration ranges of existence of different structural modifications of $Ce_{1-x}R_xAlO_3$ solutions could be established from these figures. Final results of the structural refinement of different $Ce_{1-x}La_xAlO_3$ and $Ce_{1-x}Nd_xAlO_3$ polymorphs are summarized in Table 2 and Fig. 7.

3.2.2. Phase diagrams of $CeAlO_3$–$LaAlO_3$ and $CeAlO_3$–$NdAlO_3$ pseudo-binary systems

Based on the *in situ* powder diffraction and DTA/DSC data, the phase diagrams of the $CeAlO_3$–$LaAlO_3$ and $CeAlO_3$–$NdAlO_3$ pseudo-binary systems have been constructed (Fig. 8). Besides the own experimental results, the literature data on the transition temperatures in the pure $RAlO_3$ compounds [4,15,16,20–22,28] and their melting points [44] have been used.

For both systems, the decrease of the temperatures of LT transitions is observed with decreasing cerium concentration in $Ce_{1-x}R_xAlO_3$ solid solutions. In contrast, the HT rhombohedral-to-cubic transition shows a quite different behaviour in both systems. To explain this observation, we construct the combined phase diagram for both systems,

Table 1
Crystallographic data for different structural modifications of $CeAlO_3$

Lattice parameters (Å)	Atoms, sites	x	y	z	B_{iso} (Å^2)
$T = 12$ K, S.G. $I4/mcm$, $R_I = 0.0412$; $R_P = 0.1005$; $R_{WP} = 0.1380$					
	Ce, 4*b*	0	$\frac{1}{2}$	$\frac{1}{4}$	0.16(3)
$a = 5.30945(5)$	Al, 4*c*	0	0	0	0.19(11)
$c = 7.59866(9)$	O1, 4*a*	0	0	$\frac{1}{4}$	0.9(3)
	O2, 8*h*	0.2146(11)	$x+\frac{1}{2}$	0	0.7(2)
$T = 298$ K, S.G. $I4/mcm$, $R_I = 0.0661$, $R_P = 0.1663$; $R_{WP} = 0.2043$					
$a = 5.32970(7)$	Ce, 4*b*	0	$\frac{1}{2}$	$\frac{1}{4}$	1.03(2)
$c = 7.5868(1)$	Al, 4*c*	0	0	0	1.26(10)
	O1, 4*a*	0	0	$\frac{1}{4}$	0.8(2)
	O2, 8*h*	0.2202(11)	$x+\frac{1}{2}$	0	0.9(2)
$T = 373$ K, S.G. *Imma*, $R_I = 0.0491$; $R_P = 0.1447$; $R_{WP} = 0.0971$					
$a = 5.33725(9)$	Ce, 4*e*	0	$\frac{1}{4}$	0.4968(7)	0.69(1)
$b = 7.5370(1)$	Al, 4*b*	0	0	0	0.7(15)
$c = 5.35721(8)$	O1, 4*e*	0	$\frac{1}{4}$	−0.039(3)	1.2(3)
	O2, 8*g*	$\frac{1}{4}$	−0.008(5)	$\frac{1}{4}$	0.8(15)
$T = 603$ K, S.G. $R\bar{3}c$, $R_I = 0.0414$, $R_P = 0.1428$; $R_{WP} = 0.0987$					
$a = 5.35866(7)$	Ce, 6*a*	0	0	$\frac{1}{4}$	0.75(3)
$c = 13.0868(3)$	Al, 6*b*	0	0	0	0.64(14)
	O, 18*e*	0.528(2)	$\frac{1}{4}$	0	1.9(4)
$T = 1203$ K, S.G. $R\bar{3}c$, $R_I = 0.0372$, $R_P = 0.1388$; $R_{WP} = 0.0935$					
$a = 5.3859(2)$	Ce, 6*a*	0	00	$\frac{1}{4}$	1.22(14)
$c = 13.1859(9)$	Al, 6*b*	0	0	0	0.7(8)
	O, 18*e*	0.519(3)	$\frac{1}{4}$	0	2.5(18)
$T = 1203$ K, S.G. $Pm\bar{3}m$, $R_I = 0.0343$, $R_P = 0.1177$; $R_{WP} = 0.0898$					
$a = 3.80786(3)$	Ce, 1*b*	$\frac{1}{2}$	$\frac{1}{2}$	$\frac{1}{2}$	1.29(1)
	Al, 1*a*	0	0	0	0.91(5)
	O, 3*d*	$\frac{1}{2}$	0	0	2.8(2)

on which the transition temperatures are presented as functions of the average radius of the R^{3+} cations (Fig. 9a). As evident from this diagram, the temperature of the $R\bar{3}c \leftrightarrow Pm\bar{3}m$ transition in both systems decreases linearly with increasing *R*-cation radii. This could be explained by a decrease of the perovskite structure deformation, as a consequence of the increase of the Goldschmidt tolerance factors in the series $NdAlO_3$–$CeAlO_3$–$LaAlO_3$. LT transitions show a quite different behaviour. The highest transition temperatures were observed for $CeAlO_3$. In both systems, the decrease of cerium concentration leads to the decrease of the transitions temperatures, and the dependencies are nonlinear. It is evident that in contrast to the HT $R\bar{3}c \leftrightarrow Pm\bar{3}m$ transition, LT transformations in the $CeAlO_3$-based systems are not caused by geometrical factors, but by the specific properties of the Ce^{3+} ions, i.e. their electronic structure. An absence of similar transitions in $LaAlO_3$ and $NdAlO_3$ confirms this assumption. Besides, we have prepared three samples in the $LaAlO_3$–$NdAlO_3$ system. Particularly $La_{0.62}Nd_{0.38}AlO_3$ has an average R^{3+} cation radius (1.196 Å) close to the Ce^{3+} ion. As it was shown, all three studied $La_{1-x}Nd_xAlO_3$ samples with $x = 0.2$, 0.38 and 0.7 display the rhombohedral structure at RT and undergo transitions to the cubic structure at 1070, 1350 and 1780 K, respectively. An excellent fit is observed between these data (marked with asterisks) and corresponding values for $Ce_{1-x}La(Nd)_xAlO_3$ samples (Fig. 9a). At the same time, no LT transformations were observed in $La_{1-x}Nd_xAlO_3$ solid solutions, in contrast to Ce-containing aluminates.

From the diagrams presented in Figs. 8 and 9 it is obvious, that $Ce_{1-x}R_xAlO_3$ (R = La, Nd) samples, similarly to pure $LaAlO_3$, $CeAlO_3$ and $NdAlO_3$, crystallize in the cubic perovskite structure. A continuous solid solution with the cubic HT perovskite structure exists in the $CeAlO_3$–$LaAlO_3$ system in the temperature range of about 1250–2300 K, whereas in the $CeAlO_3$–$NdAlO_3$ system such a solid solution exists in a narrow range between 2180 K and the melting point only. Other kinds of continuous solid solutions adopt the rhombohedral perovskite-like structural form in $CeAlO_3$–$La(Nd)AlO_3$ systems in the temperature ranges 430–800 and 430–1250 K, respectively. For other temperature ranges, a phase transition between different kinds of perovskite-like structures are typical. Dependencies of the perovskite cell volumes of $Ce_{1-x}R_xAlO_3$ and $La_{1-x}Nd_xAlO_3$ samples at 12, 298, 800 and 1173 K depicted in Fig. 9b confirm the complete existence of solid solutions in $CeAlO_3$–$RAlO_3$ and $LaAlO_3$–$NdAlO_3$ pseudo-binary systems.

3.2.3. *Magnetization measurements of $Ce_{1-x}La(Nd)_xAlO_3$ samples*

In Fig. 10, the temperature dependencies of the inverse magnetic susceptibility $1/\chi$ of $Ce_{1-x}La_xAlO_3$ and

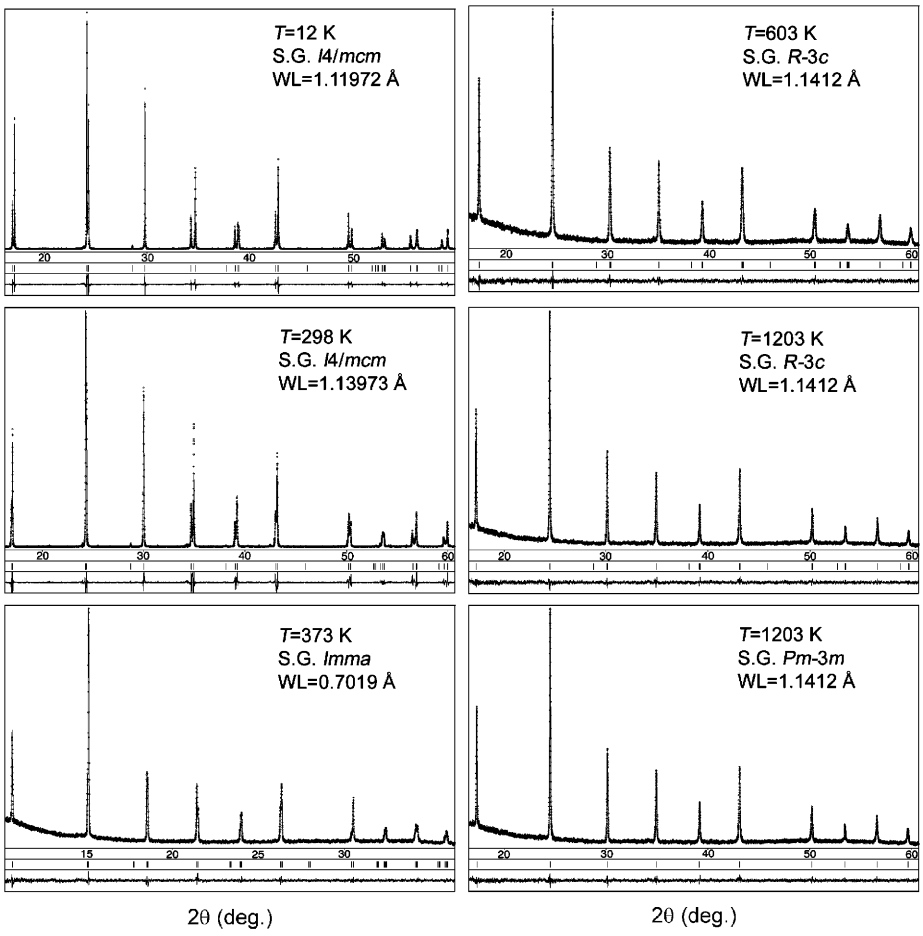

Fig. 2. High-resolution synchrotron powder diffraction patterns of different $CeAlO_3$ polymorphs at different temperatures. Parts of the patterns covering a *d*-spacing of 4.03–1.133 Å are shown. Diffraction patterns at 12 and 298 K were obtained applying a NaI scintillation detector, and all others by using the image plate OBI detector. Experimental (circles) and calculated patterns, difference profiles and positions of the diffraction maxima are given.

$Ce_{1-x}Nd_xAlO_3$ samples with $x = 0.3$, 0.5, 0.7 ($H = 1$ kOe) and 1 ($H = 10$ kOe) are presented. The curves $1/\chi(T)$ do not follow the Curie–Weiss law but show a typical curvature at LT due to the crystal field splitting of both the Ce^{3+} ($4f^1$) and Nd^{3+} ($4f^3$) magnetic states. The respective ground terms, which are almost exclusively populated in the measured temperature range, are the $^2F_{5/2}$ ($4f^1$, Ce^{3+}) and $^4I_{9/2}$ ($4f^3$, Nd^{3+}) multiplets (La^{3+} is non-magnetic). The overall splitting and the energy levels of the ground multiplet depend on the electric field gradient at the rare-earth site in the actual crystal structure. Thus, $\chi(T)$ depends on the structure, and discontinuities in $\chi(T)$ are expected at the structural phase transitions. Clear discontinuities in $\chi(T)$ are observed around 200 K in cooling and around 300 K in heating for $Ce_{0.5}La_{0.5}AlO_3$, which is in excellent agreement with the observation of the orthorhombic *Imma* phase in this temperature interval (see Fig. 5). The transitions to the *Imma* phase are of first order (vide infra). A plot of the relative difference of susceptibility data taken in heating and cooling $(\chi_\uparrow - \chi_\downarrow)/\chi_\downarrow$ (Fig. 11) reveals a large temperature hysteresis of 2–2.7% in this temperature range. With other compositions, discontinuities and temperature hystereses are less obvious. For $Ce_{0.3}La_{0.7}AlO_3$, a hysteresis is observed between 120 and 210 K, for $Ce_{0.7}La_{0.3}AlO_3$ for 250–390 K, again roughly coinciding with the existence of *Imma* structure in these temperature ranges, respectively. For the samples in the $CeAlO_3$–$NdAlO_3$ system, no remarkable hystereses are detected; however, a change of slope of $1/\chi(T)$ is discernable around 200 K in $Ce_{0.7}Nd_{0.3}AlO_3$, again in connection with the transition to the *Imma* phase (see Fig. 5). The susceptibility of the Nd-containing phases is less sensitive for changes of the crystal field.

A Curie–Weiss law fitted to $\chi(T)$ in a temperature range well above the energy splitting of the ground multiplets often yields a value of the effective magnetic moment μ_{eff} near the theoretically expected one. Calculating μ_{eff} from fits between 300 and 400 K for the samples in the $Ce_{1-x}La_xAlO_3$ system, we find 3.62 μ_B ($x = 0.7$), 2.42 μ_B ($x = 0.5$), 2.60 μ_B ($x = 0.3$), and 2.44 μ_B ($x = 0$) per Ce atom, respectively. Except the first value, μ_{eff}/Ce-atom is in the range of the theoretical value for the ground state multiplet of the $4f^1$ configuration (2.54 μ_B), suggesting the exclusive presence of trivalent cerium. The sample of $Ce_{0.3}La_{0.7}AlO_3$ was later found to be contaminated by traces of a ferromagnetic material, rendering the HT value

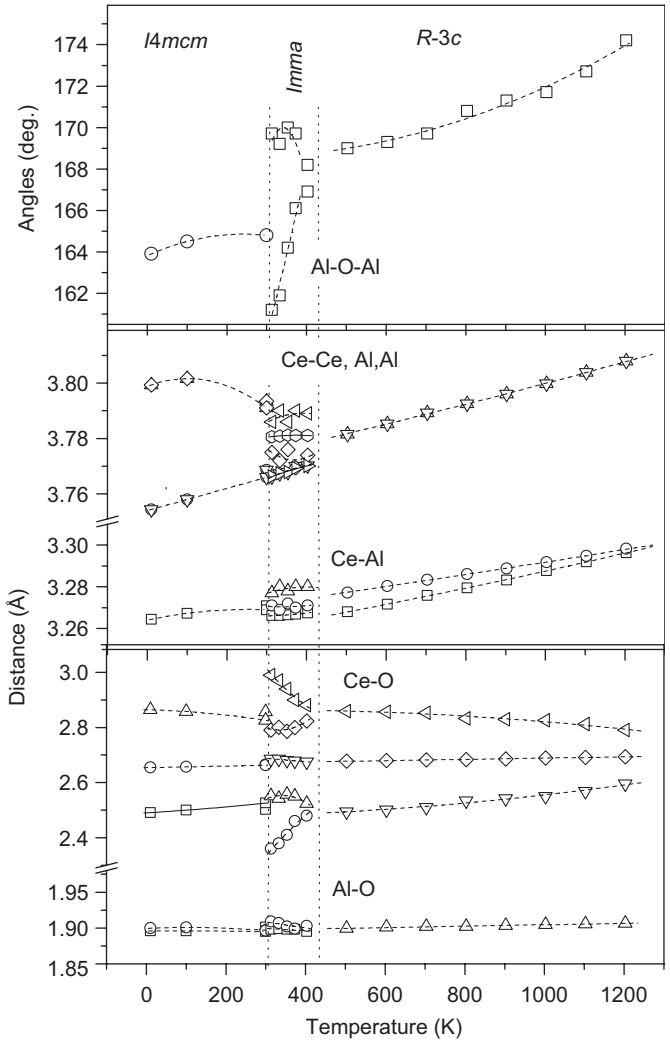

Fig. 3. Temperature dependency of selected interatomic distances and angles in $CeAlO_3$ structure.

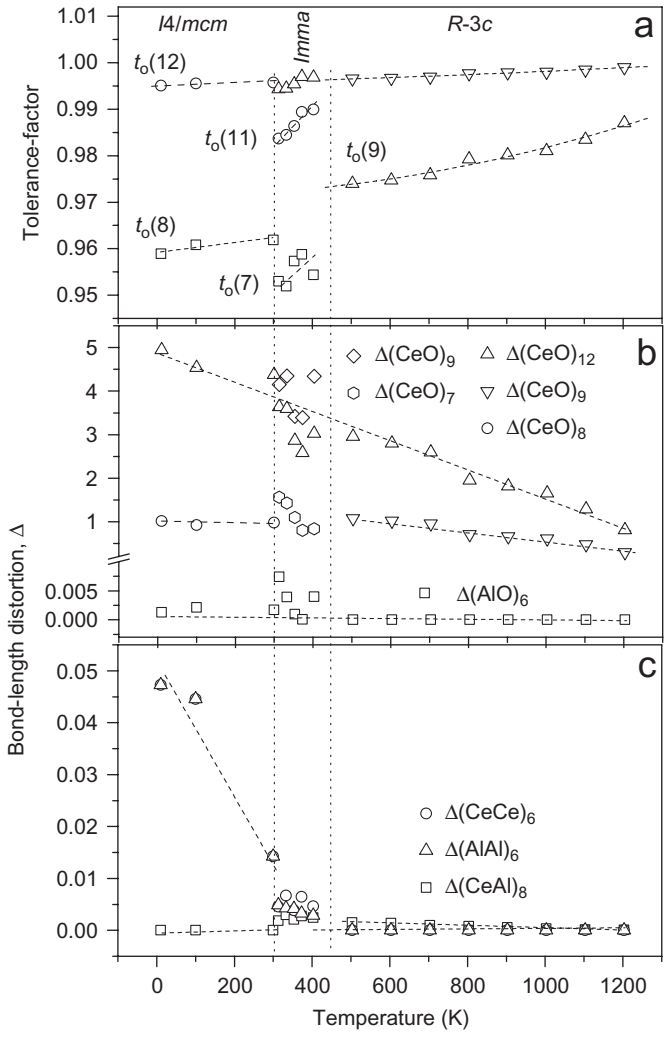

Fig. 4. Observed tolerance factor, t_o (a) and bond-length distortion of the polyhedra, Δ (b, c) in $CeAlO_3$ structure versus temperature. $\Delta = (1/n)\Sigma\{(r_i - \bar{r})/\bar{r}\}^2 \times 10^3$, where r_i and $\bar{r}$ are the individual and average values of the interatomic distances in the polyhedra with coordination number n.

of μ_{eff}/Ce atom useless. Roughly the expected moments are also observed for Curie–Weiss fits to $\chi(T)$ of samples of the $Ce_{1-x}Nd_xAlO_3$ system: 3.56 μ_B ($x = 0.7$, expected 3.33 μ_B), 3.19 μ_B ($x = 0.5$, expected 3.21 μ_B), and 2.98 μ_B ($x = 0.3$, expected 2.90 μ_B).

4. Discussion

In the ideal perovskite structure of the HT modification of $CeAlO_3$, 12 equal Ce–O and six Al–O distances are observed. The AlO_6 octahedra are regular, and octahedral axes are parallel to the four-fold $[0\,0\,1]_p$ axes of the cubic perovskite cell (Fig. 12a). According to Glazer's [45,46] notation, this structure belongs to the $a^0a^0a^0$ tilt system. For the rhombohedral $R\bar{3}c$ structure, an ideal cubooctahedron built of 12 equal Ce–O distances transforms into a polyhedron based on three shorter, six medium and three longer Ce–O bonds. In spite of all six Al–O distances remaining equal, the octahedron itself undergoes a distortion because of a deviation of the O–Al–O angles from 90°.

Rhombohedral distortion of the perovskite lattice is also reflected in the tilting of the octahedra around the three-fold $[1\,1\,1]_p$ axis. In terms of Glazer's notations, the $R\bar{3}c$ structure is characterized by anti-phase tilts of the octahedra with the same magnitude along all four-fold axes and belongs to the three-fold tilting system $a^-a^-a^-$.

In accordance with literature data, $R\bar{3}c \leftrightarrow Pm\bar{3}m$ transitions in $RAlO_3$ compounds (R = La, Pr, Nd) are ascribed to be continuous, being second-order for $LaAlO_3$ and tri-critical for $PrAlO_3$ [4]. Taking into account the temperature behaviour of the lattice parameters and cell volumes across the HT transition in $CeAlO_3$ as well as the absence of the thermal effects on the DTA/DSC curves, the continuous character of the observed transformations might be concluded. Analysis of the temperature variation of the AlO_6 octahedra tilt angles $\varphi(T)$ [26] showed that the $R\bar{3}c \leftrightarrow Pm\bar{3}m$ transition in $CeAlO_3$ is between second-order and tri-critical, closer to the latter. Similar fitting of $\varphi(T)$

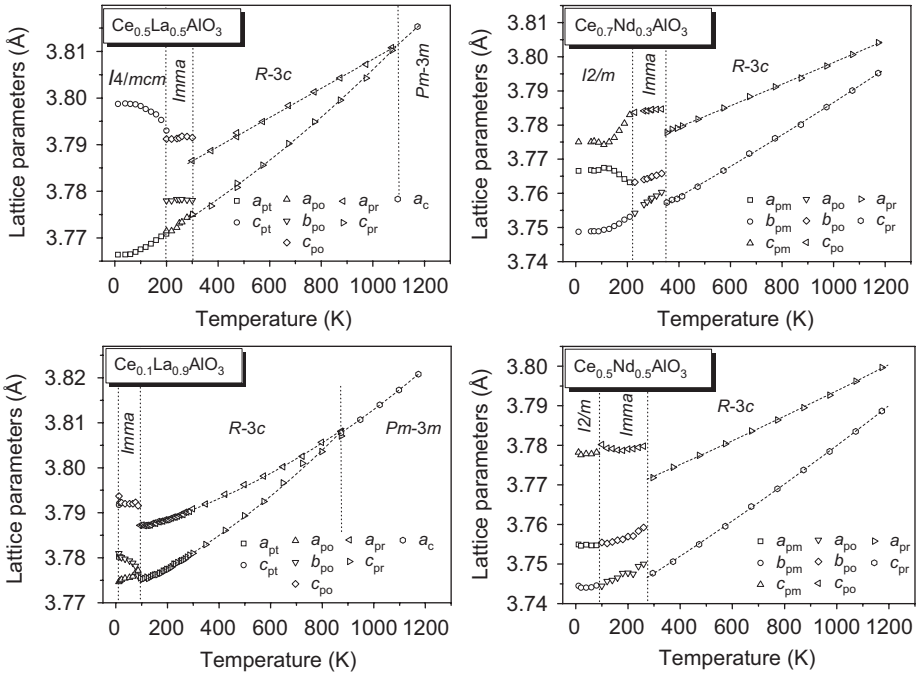

Fig. 5. Temperature dependency of the lattice parameters of $Ce_{0.1}La_{0.9}AlO_3$, $Ce_{0.5}La_{0.5}AlO_3$, $Ce_{0.5}Nd_{0.5}AlO_3$ and $Ce_{0.7}Nd_{0.3}AlO_3$. Lattice parameters of the tetragonal, orthorhombic, rhombohedral and monoclinic phases are transformed into perovskite-like pseudo-cells as follows: $a_p = a_t/\sqrt{2}$, $c_p = c_t/2$; $a_p = a_o/\sqrt{2}$, $b_p = b_o/2$, $c_p = c_o/\sqrt{2}$; $a_p = a_r/\sqrt{2}$, $c_p = c_r/\sqrt{12}$; $a_p = a_m/\sqrt{2}$, $b_p = b_m/2$, $c_p = c_m/\sqrt{2}$.

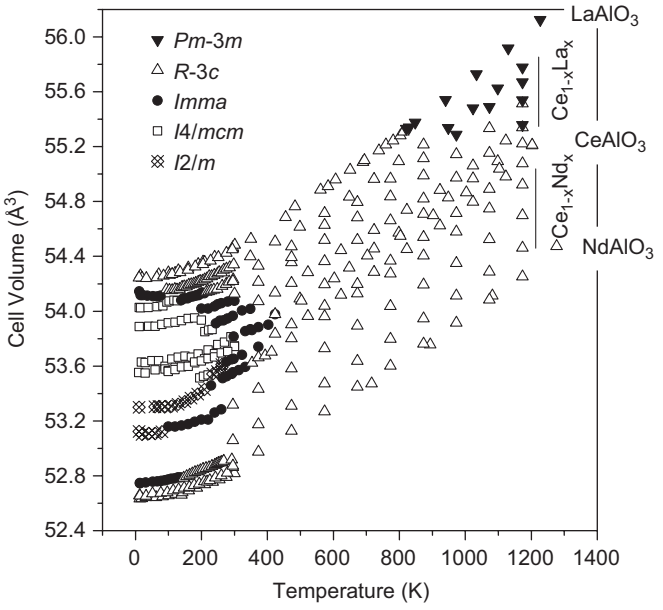

Fig. 6. Temperature dependency of the cell volumes of $LaAlO_3$, $NdAlO_3$, $CeAlO_3$ and $Ce_{1-x}R_xAlO_3$ solid solutions, normalized per one formula unit. High-temperature data for $LaAlO_3$ and $NdAlO_3$ are taken from Ref. [4].

obtained from neutron diffraction data, was performed in Ref. [28] using the formula $\varphi = A(T_c–T)^{\beta}$, where T_c is the transition temperature, and β the critical exponent. The obtained value of $\beta = 0.35$ also suggests that this transition in $CeAlO_3$ is between second-order ($\beta = 0.5$) and tri-critical character ($\beta = 0.25$).

The transition from rhombohedral to orthorhombic structure leads to a further redistribution of Ce–O and Al–O distances. There is a set of five Ce–O distances (typically grouped in 1–4–2–4–1) in the CeO_{12} polyhedra (Fig. 3). The six Al–O bonds, which have been equal in the cubic and rhombohedral structures, split into two shorter and four longer distances in the *Imma* structure, although this deformation is negligible (see Fig. 4). In the orthorhombic *Imma* structure, the octahedra undergo tilting around the two-fold $[1\,1\,0]_p$ axis or two equal anti-phase tilts along two pseudo-axes of the perovskite cell (tilt system $a^0b^-b^-$).

The next orthorhombic-to-tetragonal transition in $CeAlO_3$ is reflected in the subsequent modifications of the coordination environment of the Ce cations and in the tilt of AlO_6 octahedra. In the tetragonal $I4/mcm$ structure, the CeO_{12} polyhedra are based on four shorter, four medium and four longer bonds (Fig. 3), whereas the AlO_6 octahedra are incurred by the cooperative anti-phase rotations along the four-fold $[0\,0\,1]_p$ axis. In Glazer's notation, the tetragonal LT structure of $CeAlO_3$ and $Ce_{1-x}La_xAlO_3$ solid solutions belongs to the $a^0a^0c^-$ one-tilt system.

Both LT phase transitions in $CeAlO_3$ and $Ce_{1-x}La_xAlO_3$ solid solutions ($R\bar{3}c \leftrightarrow Imma$ and $Imma \leftrightarrow I4/mcm$) are accompanied with the changes in the cell volumes and small endothermic effects in DSC, which prove the discontinuous character of this transformations. Besides, in both cases a coexistence of LT and HT phases in the temperature ranges ± 30 K of the phase transitions has been detected. These facts and the observation of a clear temperature hysteresis in the magnetic susceptibility also point on the first-order character of both transitions.

Table 2
Crystallographic data for different structural modifications of $Ce_{1-x}La_xAlO_3$ and $Ce_{1-x}Nd_xAlO_3$ solid solutions

Lattice parameters (Å)	Atoms, sites	x	y	z	B_{iso} (Å^2)
$Ce_{0.5}La_{0.5}AlO_3$, $T = 12$ K, S.G. $I4/mcm$, $R_I = 0.0213$; $R_P = 0.1414$; $R_{WP} = 0.1550$					
$a = 5.32607(7)$	$Ce_{0.5}La_{0.5}$, 4*b*	0	$\frac{1}{2}$	$\frac{1}{4}$	0.45(3)
$c = 7.5976(1)$	Al, 4*c*	0	0	0	0.31(10)
	O1, 4*a*	0	0	$\frac{1}{4}$	0.9(3)
	O2, 8*h*	0.2211(14)	$x+\frac{1}{2}$	0	0.9(2)
$Ce_{0.5}La_{0.5}AlO_3$, $T = 250$ K, S.G. $Imma$, $R_I = 0.035$; $R_P = 0.1318$; $R_{WP} = 0.1407$					
	$Ce_{0.5}La_{0.5}$, 4*e*	0	$\frac{1}{4}$	0.5001(11)	0.68(5)
$a = 5.3432(2)$	Al, 4*b*	0	0	0	0.6(2)
$b = 7.5457(3)$	O1, 4*e*	0	$\frac{1}{4}$	−0.032(4)	1.1(6)
$c = 5.3620(2)$	O2, 8*g*	$\frac{1}{4}$	−0.018(2)	$\frac{1}{4}$	1.0(4)
$Ce_{0.5}La_{0.5}AlO_3$, $T = 473$ K, S.G. $R\bar{3}c$, $R_I = 0.055$; $R_P = 0.1358$; $R_{WP} = 0.0860$					
	$Ce_{0.5}La_{0.5}$, 6*a*	0	0	$\frac{1}{4}$	1.06(2)
$a = 5.36358(5)$	Al, 6*b*	0	0	0	0.74(9)
$c = 13.1004(2)$	O, 18*e*	0.526(2)	0	$\frac{1}{4}$	1.2(3)
$Ce_{0.5}La_{0.5}AlO_3$, $T = 1173$ K, S.G. $Pm\bar{3}m$, $R_I = 0.058$; $R_P = 0.1167$; $R_{WP} = 0.0894$					
$a = 3.81534(5)$	$Ce_{0.5}La_{0.5}$, 1*b*	$\frac{1}{2}$	$\frac{1}{2}$	$\frac{1}{2}$	1.70(3)
	Al, 1*a*	0	0	0	1.18(8)
	O, 3*d*	$\frac{1}{2}$	0	0	1.7(4)
$Ce_{0.5}Nd_{0.5}AlO_3$, $T = 12$ K, S.G. $I2/m$, $R_I = 0.0539$, $R_P = 0.1750$; $R_{WP} = 0.1683$					
	$Ce_{0.5}Nd_{0.5}$, 4*i*	0.2485(11)	0	0.7519(9)	0.38(5)
$a = 5.3103(1)$	Al, 4*e*	$\frac{1}{4}$	$\frac{1}{4}$	$\frac{1}{4}$	0.3(2)
$b = 7.4890(1)$	O1, 4*i*	0.262(7)	0	0.299(4)	0.9(7)
$c = 5.3432(1)$	O2, 4*g*	0	0.205(2)	0	0.8(8)
$\beta = 90.255(1)^\circ$	O3, 4*h*	$\frac{1}{2}$	0.237(5)	0	0.7(6)
$Ce_{0.7}Nd_{0.3}AlO_3$, $T = 298$ K, S.G. $Imma$, $R_I = 0.0757$, $R_P = 0.1429$; $R_{WP} = 0.1614$					
	$Ce_{0.7}Nd_{0.3}$, 4*e*	0	$\frac{1}{4}$	0.5010(12)	0.76(4)
$a = 5.3210(1)$	Al, 4*b*	0	0	0	0.48(8)
$b = 7.5127(1)$	O1, 4*e*	0	$\frac{1}{4}$	−0.033(5)	1.7(4)
$c = 5.3488(1)$	O2, 8*g*	$\frac{1}{4}$	−0.018(3)	$\frac{1}{4}$	1.3(2)
$Ce_{0.7}Nd_{0.3}AlO_3$, $T = 473$ K, S.G. $R\bar{3}c$, $R_I = 0.0597$, $R_P = 0.1013$; $R_{WP} = 0.0954$					
	$Ce_{0.7}Nd_{0.3}$, 6*a*	0	0	$\frac{1}{4}$	1.03(2)
$a = 5.34790(4)$	Al, 6*b*	0	0	0	0.54(7)
$c = 13.0310(1)$	O, 18*e*	0.5356(12)	$\frac{1}{4}$	0	1.3(2)

One more kind of distorted perovskite structure could be examined on the example of the monoclinic $I2/m$ structure, which was observed in the LT modification of the solid solutions existing in the $CeAlO_3$–$NdAlO_3$ system. As it was mentioned above, this rare type of perovskite structure was reported also for a LT polymorph of $PrAlO_3$ [34,35]. In the $I2/m$ structure, eight distinct Ce–O and three Al–O bond lengths develop, in sets of 1–2–1–2–2–1–2–1 and 2–2–2, respectively. Nevertheless, the deformation of octahedra remains weak, whereas 12 Ce–O distances are distributed over the range 2.42–2.92 Å. The AlO_6 octahedra are tilted about the *a*- and *c*-axis of the monoclinic cell, or, in other words, about the $[0\,1\,0]_p$ and $[0\,0\,1]_p$ axes of the ideal perovskite (tilt system $a^0b^-c^-$).

$Imma \leftrightarrow I2/m$ transitions, established in the $Ce_{1-x}Nd_xAlO_3$ samples using *in situ* synchrotron powder diffraction, were also well distinguishable by DTA, which could be treated as an indicator of their discontinuous character. The same statement could also be made for the $I2/m \leftrightarrow I4/mcm$ transition observed in $Ce_{0.9}Nd_{0.1}AlO_3$. On the other hand, the $Imma \leftrightarrow I2/m$ transformation is restricted by symmetry to be continuous [4]. A similar transition observed at 150 K in $PrAlO_3$ was already discussed in Refs. [34,35].

It is not entirely clear whether the LT phase transitions in the $CeAlO_3$-based systems have the same mechanism as it was ascribed for $PrAlO_3$ [29–35]. The sequence of phase transitions $(C2/m)I2/m \leftrightarrow Imma \leftrightarrow R\bar{3}c \leftrightarrow Pm\bar{3}m$ observed in $PrAlO_3$ and some $Pr_{1-x}La_xAlO_3$ samples have been recently interpreted in terms of strain/order parameters coupling using a simple Landau free-energy expansion for the $Pm\bar{3}m$ structure with two instabilities [35]. According to this comprehensive study, the $R\bar{3}c \leftrightarrow Imma$ transition can be understood as occurring because of coupling between tilting and electronic order-parameter components via a common tetragonal strain. Strain for the $Imma \leftrightarrow$

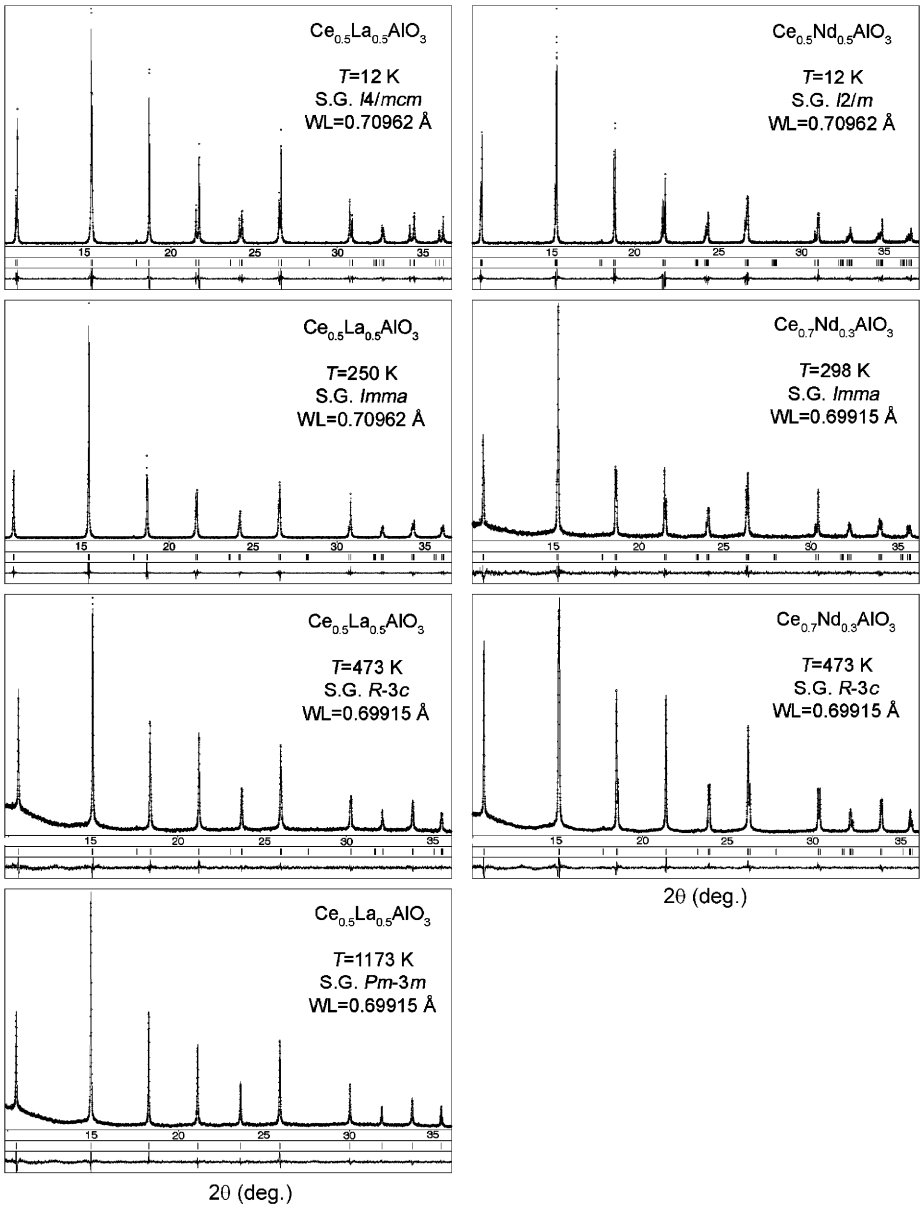

Fig. 7. High-resolution synchrotron powder diffraction patterns of $Ce_{0.5}La_{0.5}AlO_3$, $Ce_{0.5}Nd_{0.5}AlO_3$ and $Ce_{0.7}Nd_{0.3}AlO_3$ at different temperatures. Parts of the patterns covering a *d*-spacing of 4.03–1.133 Å are shown. LT diffraction patterns at 12 and 250 K were obtained by using a NaI scintillation detector, all other by using the image plate OBI detector. Experimental (circles) and calculated patterns, difference profiles and positions of the diffraction maxima are given.

*I*2/*m* transition conforms closely to the Landau solution for a proper ferroelastic transition with second-order character and LT saturation. This transition could be driven effectively by the electronic instability alone. The acoustic and optical anomalies reported in $PrAlO_3$ around 116 K [30,31,33], appear to be associated with a metrically tetragonal structure, which develops as an accidental strain degeneracy between 110 and 120 K. Moreover, LT phase transitions observed in $CeAlO_3$ and $PrAlO_3$ could be also caused by interactions between phonons and crystal field excitations of the rare-earth ions, as it was recently revealed in the related gallates $NdGaO_3$ and $PrGaO_3$, in which the pronounced anomalies in the thermal expansion were discovered [47,48].

It is interesting to note, that the sequence of phase transitions typical for $PrAlO_3$ has been observed for Ce-containing aluminates only among the samples from the $CeAlO_3$–$NdAlO_3$ system. Furthermore, the temperature dependencies of lattice parameters of $Ce_{0.7}Nd_{0.3}AlO_3$ (Fig. 5) are very similar to those reported for $PrAlO_3$ [35], including the existence of a metrically tetragonal monoclinic lattice below 110–120 K.

It is necessary to note that the monoclinic *I*2/*m* structure occurs rarely among the perovskite-type oxide. Besides $PrAlO_3$, only $BaPbO_3$, $BaPb_{0.75}Bi_{0.25}O_3$ and the $BaCe_{1-x}Y_xO_{3-z}$ solid solution have been reported to adopt this structure type [49]. Moreover, just recently the monoclinic structure in $BaPbO_3$ was disproved [50] using

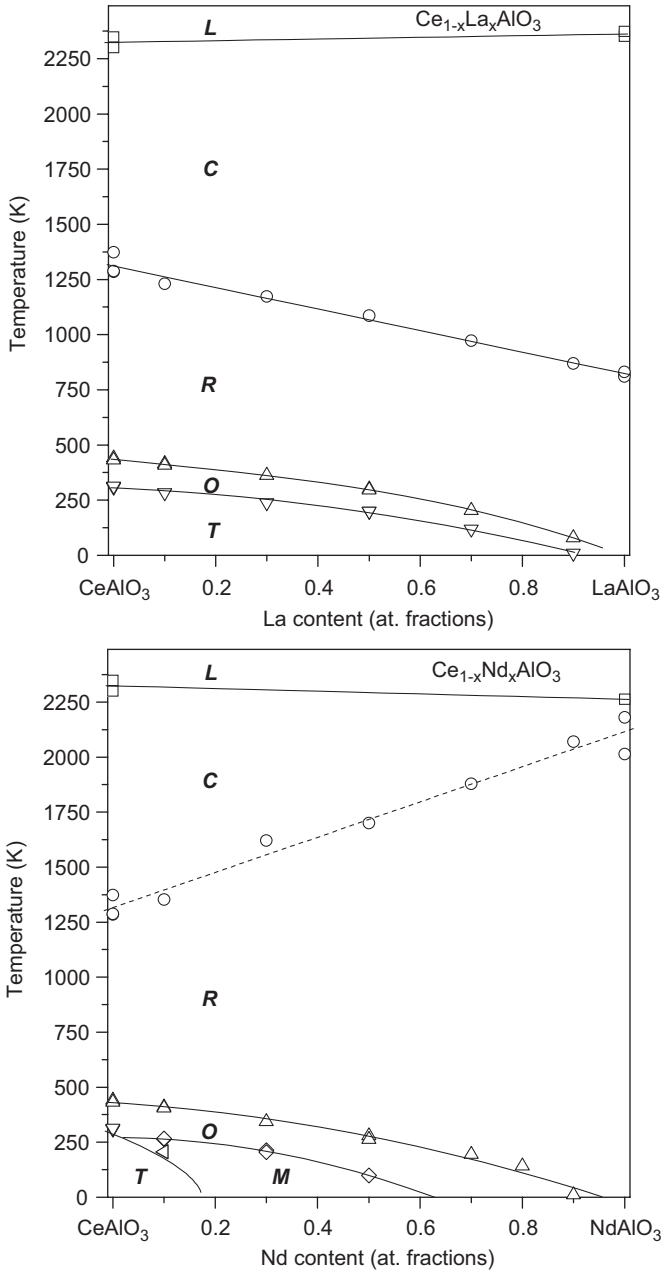

Fig. 8. Phase diagrams of the $CeAlO_3$–$LaAlO_3$ and $CeAlO_3$–$NdAlO_3$ pseudo-binary systems. The letters indicate ***L***iquid, ***C***ubic, ***R***hombohedral, ***O***rthorhombic, ***M***onoclinic and ***T***etragonal phase fields. Temperatures of the rhombohedral-to-cubic phase transitions for $Ce_{1-x}Nd_xAlO_3$ samples have been estimated from the extrapolation of the rhombohedral cell parameters ratio.

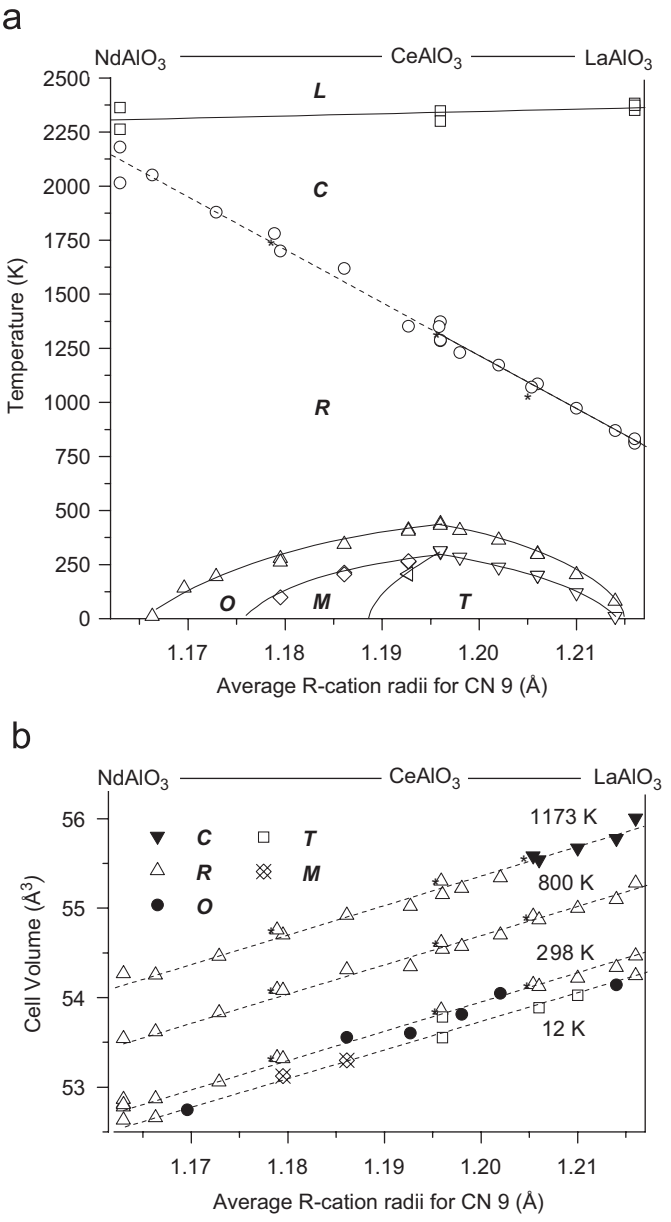

Fig. 9. Combined phase diagram of the $CeAlO_3$–$La(Nd)AlO_3$ systems (a) and cell volumes of the $Ce_{1-x}R_xAlO_3$ and $La_{1-x}Nd_xAlO_3$ solid solutions at different temperatures (b). Temperatures of the phase transformations and values of the cell volumes are given as function of the average radii of R^{3+} cations. The letters indicate ***L***iquid, ***C***ubic, ***R***hombohedral, ***O***rthorhombic, ***M***onoclinic and ***T***etragonal phases. Data for $La_{1-x}Nd_xAlO_3$ samples are marked with asterisks.

high-resolution neutron diffraction, which showed that broadening of some diffraction peaks is likely due to the presence of micro-twins. Hence, in Ref. [28] a doubt was expressed concerning the existence of the $I2/m$ monoclinic structure in $PrAlO_3$.

The tetragonal $I4/mcm$ phase observed at LT in $CeAlO_3$ and $Ce_{1-x}La_xAlO_3$ solid solutions also is the only exception among $A^{3+}M^{3+}O_3$ perovskites. In conformity with the ICSD database [49] such a structure type occurs only among $A^{2+}M^{4+}O_3$ perovskites ($BaTbO_3$ at RT, $SrTiO_3$ at LT, $SrRuO_3$, $SrZrO_3$, $SrHfO_3$ and $BaPbO_3$ at HT) and solid solutions based on them. Besides, similar structures were found among mixed manganites ($Sr_{1-x}Pr(La)_xMnO_3$), vanadites ($Sr_{1-x}Ca_xVO_3$), titanates ($CaTi_{1-x}Fe_xO_3$) and bismutates ($Sr_{1-x}K_xBiO_3$).

Given the above-described features of the cerium and praseodymium aluminates, the phase behaviour in $CeAlO_3$–$PrAlO_3$ pseudo-binary systems is expected to be very complicated. According to our preliminary investigations,

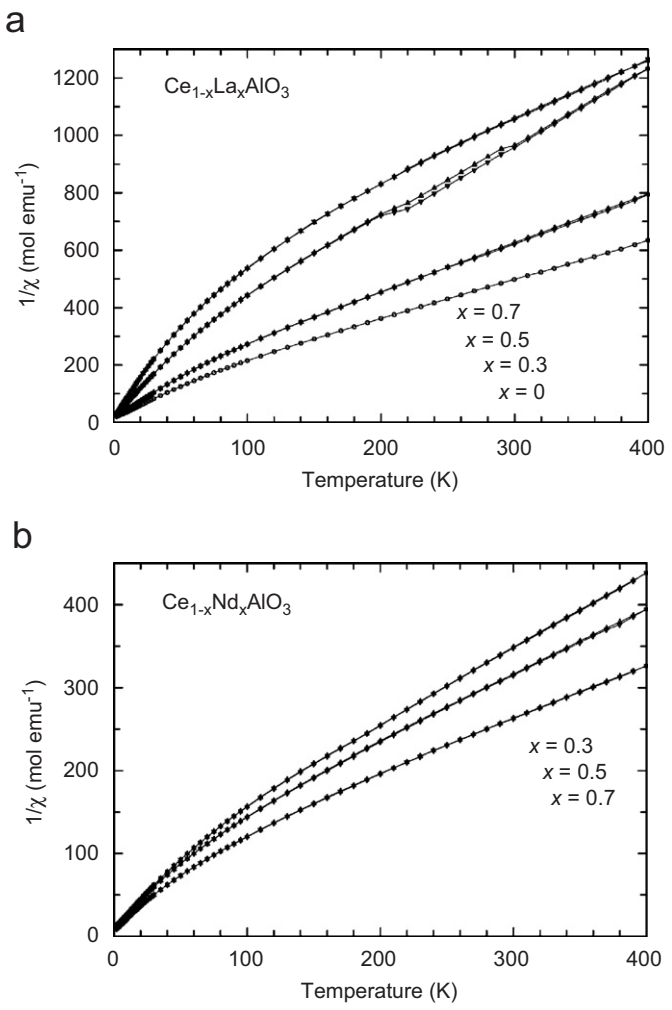

Fig. 10. Temperature dependence of the inverse magnetic susceptibility of $Ce_{1-x}La_xAlO_3$ (top) and $Ce_{1-x}Nd_xAlO_3$ (bottom) solid solutions with both increasing (triangle up) and decreasing temperature (triangle down).

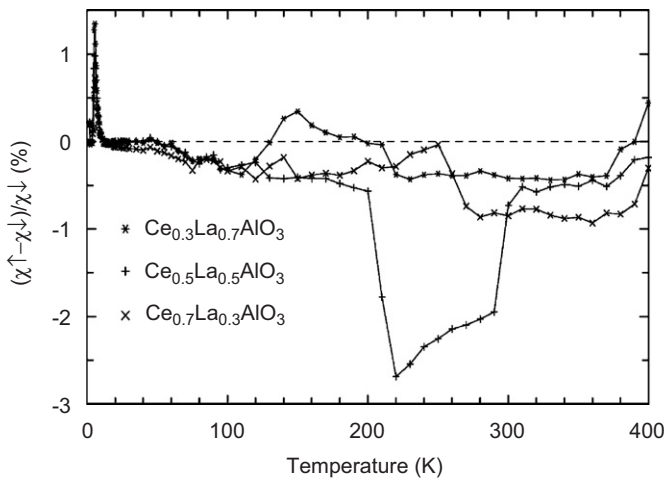

Fig. 11. Relative difference of susceptibility data $(\chi_{\uparrow}-\chi_{\downarrow})/\chi_{\downarrow}$ taken during heating (↑) and cooling (↓).

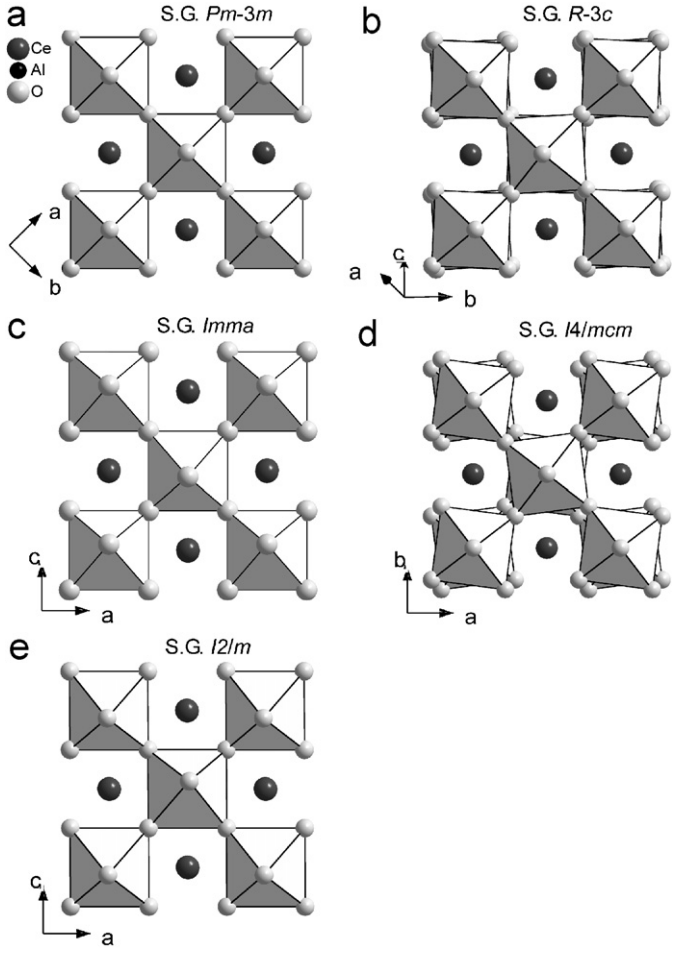

Fig. 12. Structures of the cubic, rhombohedral, orthorhombic and tetragonal polymorphs of $CeAlO_3$ (a–d) and monoclinic modification of $Ce_{0.5}Nd_{0.5}AlO_3$ (e) as a grid of AlO_6 octahedra.

five kinds of $Ce_{1-x}Pr_xAlO_3$ solid solutions with tetragonal, monoclinic, orthorhombic, rhombohedral and cubic structures were found to be existent in this system, depending on the composition and temperature [38]. The monoclinic structure appears in the samples with $x>0.1$ only in a narrow temperature range between the tetragonal and orthorhombic phase. A tentative phase diagram of the $CeAlO_3$–$PrAlO_3$ system has been proposed according to the results of *in situ* synchrotron powder diffraction and DTA/DSC data. Taking into account the revealed sequence of phase transitions $I4/mcm \leftrightarrow I2/m \leftrightarrow Imma \leftrightarrow R\bar{3}c \leftrightarrow Pm\bar{3}m$ and a subtle difference between different kinds of perovskite-like structures, a comprehensive investigation of this system applying high-resolution neutron and synchrotron powder diffraction is required, especially at the phase boundaries between tetragonal and monoclinic (pseudo-tetragonal) structures. Additional *in situ* single-crystal diffraction experiments will be also beneficial. Unfortunately, such investigations are very complicated due to the poly-domain microstructure of these materials and, hence, the difficulties in obtaining single-domain specimens suitable for data collection.

5. Conclusion

Accurate investigations of cerium aluminate $CeAlO_3$ and solid solutions based on it are performed in a wide temperature range of 12−1200 K by a combination of *in situ* high-resolution X-ray powder diffraction technique applying synchrotron radiation, thermal analysis and magnetization measurements. Performed research efforts allowed to establish the complicate behaviour of the phase transformations occurring in $CeAlO_3$–$LaAlO_3$ and $CeAlO_3$–$NdAlO_3$ pseudo-binary systems. For the $Ce_{1-x}La_xAlO_3$ samples, like for pure $CeAlO_3$, the following sequence of the reversible phase transitions has been found: $I4/mcm \leftrightarrow Imma \leftrightarrow R\bar{3}c \leftrightarrow Pm\bar{3}m$. In the $CeAlO_3$–$NdAlO_3$ system, the $Ce_{1-x}Nd_xAlO_3$ compositions with $x = 0.3$ and 0.5 display the reversible transformations $I2/m \leftrightarrow Imma \leftrightarrow R\bar{3}c \leftrightarrow Pm\bar{3}m$, similar to the ones described earlier in $PrAlO_3$. Finally, for the Ce-rich $Ce_{0.9}Nd_{0.1}AlO_3$ sample, four successive transitions are observed: $I4/mcm \leftrightarrow I2/m \leftrightarrow Imma \leftrightarrow R\bar{3}c \leftrightarrow Pm\bar{3}m$. Phase diagrams of the $CeAlO_3$–$LaAlO_3$ and $CeAlO_3$–$NdAlO_3$ pseudo-binary systems and a combined phase diagram, in which the transition temperatures are depicted as a function of the average radius of rare-earth cations, are constructed.

Crystal structures of all polymorphs of $CeAlO_3$ and $Ce_{1-x}R_xAlO_3$ solid solutions have been established and their thermal evolution in a wide temperature range of 12−1200 K are described. The magnetic susceptibility of these phases is compatible with the crystal field ground states for La^{3+}, Ce^{3+}, and Nd^{3+} ions, respectively. The first-order phase transitions involving the *Imma* phase are clearly seen in a temperature hysteresis of the susceptibility.

Seventeen experimental powder diffraction patterns of different structural modifications of $CeAlO_3$, $Ce_{1-x}La_xAlO_3$ and $Ce_{1-x}Nd_xAlO_3$ collected *in situ* at different temperatures, have been recently published by the International Centre of Diffraction Data (ICDD) in the release 2005 of the Powder Diffraction File (PDF cards NN 55–890, 55–889, 55–676, 55–961 and 55–633) and 2006 (PDF cards NN 56–240, 56–243, 56–244, 56–246, 56–323, 56–324, 56–327, 56–419, 56–420, 56–1373, 56–1391 and 56–1392).

Acknowledgments

The work was supported in parts by WTZ (UKR-01/12 and UKR-04/007), the Ukrainian Ministry of Education and Science and ICDD Grant-in-Aid programme. L. Vasylechko acknowledges the Max-Planck Society for a research fellowship. The authors are thankful to S. Fadeev and I. Saldan for their assistance during the preparation of samples.

References

[1] S. Geller, V.B. Bala, Acta Crystallogr. 9 (1956) 1019–1025.
[2] P.D. Dernier, R.G. Maines, Mater. Res. Bull. 6 (1971) 433–440.
[3] T. Shishido, S. Nojima, M. Tanaka, H. Horiuchi, T. Fukuda, J. Alloy Compd. 227 (1995) 175–179.
[4] C.J. Howard, B.J. Kennedy, B.C. Chakoumakos, J. Phys.: Condens. Matter 12 (2000) 349–365.
[5] G. Cruciani, F. Matteucci, M. Dondi, G. Baldi, A. Barzanti, Z. Kristallogr. 220 (2005) 930–937.
[6] W.H. Zachariasen, Acta Crystallogr. 2 (1949) 388–390.
[7] M.L. Keith, R. Roy, Am. Miner. 39 (1-2) (1954) 1–23.
[8] R.S. Roth, J. Res. Natl. Bur. Stand. 58 (2) (1957) 75–88.
[9] Y.S. Kim, Acta Crystallogr. B 24 (1968) 295–296.
[10] M. Mizuno, T. Yamada, T. Noguchi, Y. Kyokaishi, J. Ceram. Soc. Japan 83 (2) (1975) 90–96.
[11] A.I. Leonov, Izv. Akad. Nauk SSSR. Otd. Khim. Nauk 1 (1963) 8–13 (in Russian).
[12] N. Kaufherr, L. Mendelovici, M. Steinberg, J. Less Common Met. 107 (1985) 281–289.
[13] M. Tanaka, T. Shishido, H. Horiuchi, N. Toyota, T. Shindo, T. Fukuda, J. Alloys Compd. 192 (1993) 87–89.
[14] A.C. Tas, M. Akinc, J. Am. Ceram. Soc. 77 (11) (1994) 2961–2967.
[15] T. Shishido, Y. Zheng, A. Saito, H. Horiuchi, K. Kudou, S. Okada, T. Fukuda, J. Alloys Compd. 260 (1997) 88–92.
[16] A.I. Shekych, N.S. Zhdanovich, B.T. Melekh, N.F. Kartenko, Yu.N. Filin, A.V. Prokofyev, I.A. Smirnov, Phys. Solid State (Russ. Fiz. Tverd. Tela) 36 (3) (1994) 817–821 (in Russian).
[17] A.I. Shelykh, B.T. Melekh, Phys. Solid State 45 (2) (2003) 248–251.
[18] S. Okada, K. Kudou, K. Izumi, K. Nakajima, T. Shishido, Kokushikan Daigaku Rikogaku Kenkyusho Hokoku (Bull. Sci. Eng. Res. Inst. Kokushikan Univ.) 16 (2004) 23–26.
[19] S. Tozawa, T. Shishido, M. Tanaka, T. Sasaki, T. Chiba, S. Oishi, K. Machida, N. Kamegashira, H. Horiuchi, K. Nakajima, Gijutsubu Gijutsu Kenkyu Hokoku (Tech. Rep. Inst. Met. Res. Tohoku Univ. 20 (2003) 33–35 (in Japanese).
[20] A.I. Leonov, A.B. Andreeva, V.E. Shvaiko-Shvaikovskii, E.K. Keller, Izv. Akad. Nauk SSSR, Neorg. Mater 2 (3) (1966) 517–523 (in Russian).
[21] A.I. Leonov, High-temperature chemistry of cerium oxide compounds. Handbook. Nauka, Leningrad (1970) 199 (in Russian).
[22] S. Geller, P.M. Raccah, Phys. Rev. B 2 (1970) 1167–1172.
[23] V.M. Egorov, Yu.M. Baikov, N.F. Kartenko, B.T. Melekh, Yu.N. Filin, Phys. Solid State 40 (11) (1998) 1911–1914.
[24] L. Vasylechko, R. Niewa, A. Senyshyn, Y. Pivak, D. Savytskii, M. Knapp, C. Bähtz, HASYLAB Ann. Rep. 1 (2002) 223–224.
[25] L. Vasylechko, R. Niewa, W. Schnelle, A. Senyshyn, M. Knapp, in: Proceedings of Ninth European Conference on Solid State Chemistry, ECSSC-9. Stuttgart, Germany, September 3–6, 2003. P049.
[26] L.O. Vasylechko, A.O. Matkovskii, Bull. Lviv Polytech. Natl. Univ., Electronics 514 (2004) 33–52 (in Ukrainian).
[27] W.T. Fu, D.J.W. IJdo, J. Solid State Chem. 177 (2004) 2973–2976.
[28] W.T. Fu, D.J.W. IJdo, J. Solid State Chem. 179 (2006) 2732–2738.
[29] R.D. Burbank, J. Appl. Crystallogr. 3 (1970) 112–120.
[30] W.A. Nordland, L.G. Van Uitert, J. Phys. Chem. Solids. 31 (6) (1970) 1257–1262.
[31] R.T. Harley, W. Hayes, A.M. Perry, S.R.P. Smith, J. Phys. C: Solid State Phys. 6 (1973) 2382.
[32] R.J. Birgeneau, J.K. Kjems, G. Shirane, L.G. Van Uitert, Phys. Rev. B 10 (1974) 2512–2534.
[33] H. Fujii, M. Hidaka, B.M. Wanklyn, Phase Transitions 70 (1999) 115–132.
[34] S.M. Moussa, B.J. Kennedy, B.A. Hunter, C.J. Howard, T. Vogt, J. Phys.: Condens. Matter 13 (2001) L203–L209.
[35] M.A. Carpenter, C.J. Howard, B.J. Kennedy, K.S. Knight, Phys. Rev. B 72 (2005) 024118.
[36] L. Vasylechko, S. Fadyeev, D. Trots, A. Senyshyn, R. Niewa, W. Schnelle, M. Knapp, HASYLAB Ann. Rep. 1 (2003) 255–256.
[37] L. Vasylechko, S. Fadeyev, R. Niewa, W. Schnelle, M. Knapp, U. Bismayer, HASYLAB Ann. Rep. 1 (2003) 399–400.

[38] L. Vasylechko, R. Niewa, A. Senyshyn, D. Trots, U. Bismayer, M. Knapp, C. Bähtz, S. Fadyeev, HASYLAB Ann. Rep. 1 (2004) 323–324.
[39] L. Vasylechko, S. Fadyeev, R. Niewa, W. Schnelle, M. Knapp, in: Proceedings of International Conference "Perovskites–Properties and Potential Applications", Dübendorf, Switzerland, 2005, p. 135.
[40] M. Knapp, V. Joco, C. Bähtz, H.H. Brecht, A. Berghäuser, H. Ehrenberg, H. von Seggern, H. Fuess, Nucl. Instrum. Methods A 521 (2004) 565.
[41] J. Ihringer, A. Kuester, J. Appl. Crystallogr. 26 (1993) 135–137.
[42] L.G. Akselrud, P.Yu. Zavalij, Yu. Grin, V.K. Pecharsky, B. Baumgartner, E. Woelfel, Mater. Sci. Forum 133–136 (1993) 335.
[43] S. Sasaki, C.T. Prewitt, R.C. Liebermann, Am. Miner. 68 (1983) 1189.
[44] P. Wu, D. Pelton, J. Alloys Compd. 179 (1992) 259–287.
[45] A.M. Glazer, Acta Crystallogr. B 28 (1972) 3384–3392.
[46] A.M. Glazer, Acta Crystallogr. A 31 (1975) 756–762.
[47] D. Savytskii, L. Vasylechko, A. Senyshyn, A. Matkovskii, C. Bähtz, M.L. Sanjuan, U. Bismayer, M. Berkowski, Phys. Rev. B 68 (2003) 024101.
[48] L. Vasylechko, Ye. Pivak, A. Senyshyn, D. Savytskii, M. Berkowski, H. Borrmann, M. Knapp, C. Paulmann, J. Solid State Chem. 178 (2005) 270–278.
[49] Inorganic Crystal Structure Database. Version 2005-2. Fachinformationszentrum (FIZ) Karlsruhe, Germany and National Institute of Standards and Technology (NIST), USA.
[50] W.T. Fu, D. Wisser, K.S. Knight, D.J.W. IJdo, J. Solid State Chem. 177 (2004) 1667.